Accepted to Phys. Fluids 10.1063/5.0180850

Hysteresis phenomenon of the sloshing mode resonance in a moonpool induced by rolling motion excitations

Sheng-Chao JIANG[a], Wei Bai[b], Lin LU[c]

[a] *School of Naval Architecture, Dalian University of Technology, Dalian 116024, China*
[b] *Department of Computing and Mathematics, Manchester Metropolitan University, Chester Street, Manchester M1 5GD, UK*
[c] *State Key Laboratory of Coastal and Offshore Engineering, Dalian University of Technology, Dalian 116024, China*

Abstract

Sloshing-mode resonance in the moonpool induced by roll motion excitations is investigated numerically using the OpenFOAM® package. Nonlinear characteristics of the sloshing-mode resonance are the main focus of the present study. When the roll motion excitation has a time-invariant amplitude, a typical softening spring behaviour can be observed in the variation of free surface amplitude against the excitation frequency, including the decreased resonant amplitude and the jump frequency. Furthermore, the dimensionless jump frequency is independent of the moonpool breadth and draft in this situation. The hysteresis phenomenon is clearly observed under the roll excitation with varying amplitudes, where the phase locked-in mechanism is the essential reason for this phenomenon. The hysteresis loop is located between two jump frequencies by the accelerating and decelerating excitations that generate the lower and upper branches, respectively. With the increase of moonpool breadth, the decreased upper branch frequency and unchanged lower branch frequency are observed, leading to the increased region of the hysteresis loop. The variation of the moonpool draft has an insignificant effect on the region of the hysteresis loop.

Keywords: Hysteresis, Fluid resonance, Moonpool, Roll motion excitation, OpenFOAM®

1. Introduction

Moonpool is a vertical opening through the deck of offshore structures or the hull of ships. With the rapid increase in the development of subsea industry, the use of moonpools to perform marine operations is expected to grow significantly. Marine operators have defined goals for the operation, such as the near all-year availability for maintenance and repair, and the required operability in severe wave conditions. Specialized offshore vessels with moonpools are regarded as one of the key elements to achieve these goals. However, the fluid inside the moonpool may experience large-amplitude piston- and sloshing-mode resonances under certain wave conditions. The piston-mode resonance features with the free surface heaving up and down like a solid body; while the sloshing-mode resonance is alike the fluid motion inside a sloshing tank. Therefore, careful design of the moonpool is required to avoid the hazard from the fluid resonance, which is one of the main technical challenges in practical engineering.

Fluid resonance in the moonpool can be considered as the eigenvalue of the corresponding boundary value problem. Molin (2001) derived an analytical solution for the fluid resonance in a moonpool via solving

Accepted to Phys. Fluids 10.1063/5.0180850

an eigenvalue equation based on the linearized potential flow theory, where the piston- and sloshing-mode resonant frequencies correspond to the fundamental and higher eigenfrequencies, respectively. Faltinsen et al. (2007) reported a semi-analytical method for the two-dimensional piston-like sloshing resonance in the moonpool. Zhang et al. (2019) proposed a theoretical model for computing the natural frequencies and modal shapes of two-dimensional asymmetric and symmetric moonpools in the finite water depth. An experimental measurement was conducted by Fredriksen et al. (2014) to investigate the fluid resonance in a moonpool undergoing heave motion oscillations. Jiang et al. (2019a) and Jiang et al. (2021) simulated the wave resonance in a moonpool formed by the box-wall and two-box systems, respectively. The behaviour of piston-like oscillation by the first-, second- and third-order harmonic components was investigated. According to several studies during the past decades, it is established that fluid viscosity and flow rotation play an important role in the behaviour of fluid resonance in the moonpool.

With the development of computing techniques, Computational Fluid Dynamics (CFD) simulations have been widely applied to the fluid resonance problem. Fredriksen et al. (2015) investigated the hydrodynamic behaviour of a two-dimensional freely floating vessel with a moonpool under wave actions. Feng et al. (2017) performed three-dimensional simulations for two side-by-side barges by using a viscous fluid flow wave flume. Gao et al. (2019) investigated the hydrodynamic behaviour of a two-box system, by which the harmonic analysis of the free surface elevation in the moonpool and wave load on the bodies was conducted. Lu et al. (2020) considered the influence of mooring stiffness on the fluid resonance in the narrow gap formed by a box-wall system. Numerical simulations were also carried out by Jing et al. (2022) for the fluid resonance of a heaving-free moonpool in a wide range of incident waves. Moreover, the essential mechanism of fluid resonance in the moonpool can be revealed based on the detailed simulations and discussions. Faltinsen and Timokha (2015) quantified a pressure discharge condition in the moonpool opening for considering the damping mechanism. Jiang et al. (2018) investigated the wave reflection and transmission coefficients as well as the energy coefficient around the resonant frequency, by which the mechanical essence of the gap resonance problem was discussed from the perspective of energy dissipation and energy transformation. Tan et al. (2019) proposed a viscous damping model for fluid resonance in the moonpool, where the damping induced by the flow separation and wall friction was considered by the local and frictional loss coefficients, respectively. Milne et al. (2022) conducted a series of experimental measurements on the fluid resonance problem, and the vortex shedding from the sharp bilge edge is demonstrated to give rise to a quadratically damped free surface resonance.

The above-mentioned research efforts mainly focused on the piston-mode resonance problem; while the sloshing-mode resonance has attracted relatively less attention. Molin et al. (2018) adopted an eigenfunction expansion and Garrett's method for the circular and rectangular moonpool problem, by which the sloshing-mode natural frequencies and associated modal shapes were formulated. Chu and Zhang (2021) established the theoretical model for sloshing-mode resonance in the moonpool with one or two recesses in the finite water depth. Zhang and Li (2022) analysed the fluid resonance in a three-dimensional rectangular and

Accepted to Phys. Fluids 10.1063/5.0180850

circular moonpool with recesses by an eigenfunction expansions method. Jiang et al. (2023) investigated the behaviour of the second-order harmonic induced sloshing-mode resonance in the moonpool, where the notable peak value appears due to the superposition of piston- and sloshing-mode resonances. There are some similar features between the liquid sloshing in tanks and the sloshing-mode resonance in moonpools. Therefore, the nonlinear behaviour of liquid sloshing in tanks is an important reference to the study of sloshing-mode resonance in moonpools. Faltinsen et al. (2000) systematically investigated the behaviour of liquid sloshing problem, where the nonlinear characteristics can be confirmed analytically and experimentally. Ockendon and Ockendon (2001) described the influence of nonlinearity on the liquid sloshing in tanks by using a nonlinear mass-spring equation. Nonlinear behaviour in the liquid sloshing problem can be explained by a cubic term in the nonlinear mass-spring system. In fact, the first and most popular nonlinear mass-spring model was established by Duffing (1918) over a hundred years ago. In order to describe the dependence of resonant frequency on the driving amplitude, the cubic nonlinear term is added to the classical harmonic driven oscillator. The resulting (Duffing) equation reads,

$$\ddot{x} + 2\delta\dot{x} + \omega_n^2 x + \varepsilon x^3 = F\cos\omega t, \tag{1}$$

where F and ω are the excitation amplitude and excitation frequency of the harmonic driven system. x is the displacement of the oscillation, δ is the viscous damping coefficient, and ω_n is the natural frequency. ε is the coefficient of the nonlinear term, which is a constant in this equation. Depending on the sign of the parameter ε, the nonlinear resonant frequency shifts to a value lower than that of a linear mass-spring system for a softening spring ($\varepsilon < 0$) or a higher value for a hardening spring ($\varepsilon > 0$). The shift of the resonance frequency and the corresponding bending of the resonance curve are the key features of Eq. (1) (see Kovacic and Brennan 2011 for a monograph on the Duffing equation). Fig. 1 shows the sketch of the behaviour of a linear spring ($\varepsilon = 0$), a softening spring ($\varepsilon < 0$) and a hardening spring ($\varepsilon > 0$). Furthermore, the solid and dashed lines in the figure stand for the stable and unstable parts in the softening and hardening spring solutions, respectively. In practical engineering, the response abruptly changes between the stable and unstable solutions at a certain frequency that is commonly called the jump frequency (dash-dot lines in the figure).

Several previous work was developed for the nonlinear sloshing flow motion based on the above mass-spring theory. Hill (2003) conducted a weakly nonlinear analysis for the transient evolution of two-dimensional standing waves in a rectangular basin. The hardening spring behaviour of sloshing flow was formulated in the water of general depth, which is valid for the ratio of the water depth to the tank length above the 'critical depth' (0.162). Gardarsson and Yeh (2007) explored the liquid sloshing behaviour in the shallow water depth, experimentally. It was observed that the nonlinear characteristics of sloshing responses in the rectangular tank and the sloping bottom tank behave like the hardening and softening springs, respectively. Gurusamy and Kumar (2020) performed the experimental study on the nonlinear sloshing frequency in the shallow water depth. Nonlinear characteristics such as the resonance shift and jump frequency were reported, where the resonant frequency affected by the nonlinearity is sensitive to the excitation amplitude and the

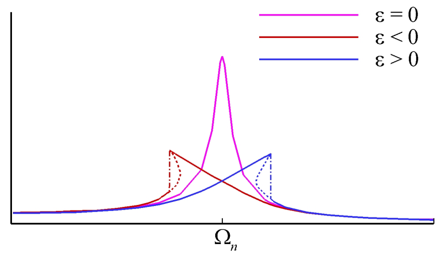

Figure 1: Typical amplitude-frequency curves for the Duffing equation with different nonlinear term coefficients.

ratio of the water depth to the tank length. Based on the nonlinear vibration theory, the sudden change at the jump frequency is associated with the phenomena of hysteresis. Hysteresis is the name of a system where the output depends on not only the input but also the history of past inputs. The bifurcation, which is the origin of hysteresis, results from the cubic term in the nonlinear mass-spring equation. It is speculated that the phenomenon of hysteresis can be found in the liquid sloshing problem. Gurusamy and Kumar (2020) conducted the laboratory measurement for the hysteresis of the liquid sloshing in rectangular and sloping bottom tanks in the condition that the ratio of the water depth to the tank length is 0.038. The modal characteristics of hydraulic jumps in the sloshing flow of shallow water depth were further investigated in Gurusamy et al. (2021). Liu et al. (2022) estimated the influence of the length scale on the Kelvin-Helmholtz instabilities by using the critical Richardson number. An experimental measurement by Bäuerlein and Avila (2021) showed the low-amplitude sloshing obeys the Duffing equation. A bending of the response curve in analogy to a softening spring was observed, with the growing hysteresis as the driven amplitude increases. Miliaiev and Timokha (2023) further investigated the viscous damping effect on the nonlinear sloshing flow motion. It was confirmed that the free surface nonlinearity and viscous damping of the higher natural sloshing modes matter, as well as that the damping rates can depend on the steady-state wave amplitude. The above efforts indicated that hysteresis has a significant effect on the behaviour of sloshing flow motion, which can also further affect the relevant phenomena such as the jump frequency and wave amplitude.

The previous investigations on the nonlinear behaviour were mainly for the liquid sloshing problem in tanks; whereas, to the best of the authors' knowledge, no studies on the nonlinear behaviour have been reported for the moonpool problem. The sloshing-mode resonance in the moonpool exhibits similar characteristics to the liquid sloshing problem. Therefore, it is believed that the nonlinear behaviour in the liquid sloshing in tanks may also appear in the sloshing-mode resonance in the moonpool, which is the motivation of this study. In the present work, the sloshing-mode resonance induced by rolling motion excitations is investigated. Nonlinear free surface responses in the moonpool are simulated and analysed. The softening spring behaviour of the free surface amplitudes in the moonpool induced by fixed-amplitude roll motions is reported.

Hysteresis phenomena are revealed for the first time by increasing and decreasing the roll motion amplitude near the resonant condition, which can significantly affect the free surface elevation in the moonpool around the resonant frequency.

2. Mathematical Formulation

The governing equations for the mass and momentum conservations in incompressible turbulent flows with a Re-Normalization Group (RNG) model in the Arbitrary Lagrangian-Eulerian (ALE) reference system can be given as,

$$\frac{\partial \rho}{\partial t} + \frac{\partial \rho u_i}{\partial x_i} = 0, \tag{2a}$$

$$\frac{\partial \rho u_i}{\partial t} + \frac{\partial \rho (u_j - u_j^m) u_i}{\partial x_j} = \rho f_i - \frac{\partial p}{\partial x_i} + \mu_e \frac{\partial}{\partial x_j}\left(\frac{\partial u_i}{\partial x_j} + \frac{\partial u_j}{\partial x_i}\right), \tag{2b}$$

where u_i is the velocity component in the ith direction, u_i^m is the velocity component due to the mesh deformation in the ALE frame. p, ρ and f_i are the pressure, fluid density and external body force, respectively. μ_e is the effective dynamic viscosity with $\mu_e = \mu_m + \mu_t$, μ_m the fluid molecule viscosity and μ_t the turbulent viscosity. The RNG $k-\varepsilon$ two-equation formulations are adopted for closing the governing equations, which gives rise to,

$$\mu_t = C_\mu \frac{k^2}{\varepsilon}, \tag{3}$$

where $C_\mu = 0.09$ is a theoretical model constant, and the time-dependent advection-diffusion equations for the turbulent kinematic energy k and its dissipation rate ε can be written as,

$$\frac{\partial \rho k}{\partial t} + \frac{\partial \rho (u_j - u_j^m) k}{\partial x_j} = \frac{\partial}{\partial x_j}\left(\frac{\mu_t}{\sigma_k}\frac{\partial k}{\partial x_j}\right) + \mu_t\left(\frac{\partial u_i}{\partial x_j} + \frac{\partial u_j}{\partial x_i}\right)\frac{\partial u_i}{\partial x_j} - \rho\varepsilon, \tag{4a}$$

$$\frac{\partial \rho \varepsilon}{\partial t} + \frac{\partial \rho (u_j - u_j^m) \varepsilon}{\partial x_j} = \frac{\partial}{\partial x_j}\left(\frac{\mu_t}{\sigma_\varepsilon}\frac{\partial \varepsilon}{\partial x_j}\right) + C_{1\varepsilon}\frac{\varepsilon}{k}\mu_t\left(\frac{\partial u_i}{\partial x_j} + \frac{\partial u_j}{\partial x_i}\right)\frac{\partial u_i}{\partial x_j} - \rho C_{2\varepsilon}\frac{\varepsilon^2}{k}, \tag{4b}$$

where the model constants $C_{1\varepsilon}$, $C_{2\varepsilon}$, σ_k and σ_ε are 1.42, 1.68, 0.71942 and 0.71942, respectively. Note that the model constants are derived theoretically in the RNG turbulent model (Yakhot and Orszag, 1986; Yakhot and Smith, 1992).

The Volume of Fluid (VOF) method (Hirt and Nichols, 1981) is adopted in this work to capture the free surface motion. The fractional function of VOF, denoted by φ, in a computational cell is defined as,

$$\varphi = \begin{cases} 0, & \text{in air,} \\ 0 < \varphi < 1, & \text{on free surface,} \\ 1, & \text{in water.} \end{cases} \tag{5}$$

It satisfies the following advection equation,

$$\frac{\partial \varphi}{\partial t} + (u_i - u_i^m)\frac{\partial \varphi}{\partial x_i} = 0. \tag{6}$$

In this work, the contour of the fractional function with $\varphi = 0.5$ is used to represent the interface between the water and air phases. In the computations, the fluid density and effective viscosity are averaged by using the available frictional function,

$$\rho = \varphi\rho_W + (1-\varphi)\rho_A, \tag{7a}$$

$$\mu_e = \varphi\mu_{eW} + (1-\varphi)\mu_{eA}, \tag{7b}$$

where the subscripts W and A represent the water phase and air phase, respectively.

In the present numerical wave flume, the reflection wave is eliminated by means of a spongy layer. That is, an artificial damping force is introduced in the body force term of Eq. (2b),

$$f_i = g_i + R_i \tag{8}$$

where g_i is the gravitational acceleration, and R_i is the artificial damping force. Note that the damping force is only activated in the vertical direction y for the present two-dimensional problem for the sake of numerical stability. Herein, the horizontal component is $R_x = 0$, while the vertical component R_y takes the following form (Lu et al., 2010),

$$R_y = -k_s\left(\frac{x-x_0}{D_s}\right)^2 \frac{y_b - y}{y_b - y_h} \cdot v \tag{9}$$

where x and y are the Cartesian coordinates of the node, x_0 is the coordinate of the starting point of the spongy layer, v is the vertical velocity component, y_b is the elevation of the seabed and y_h is the flume height. k_s is an empirical parameter determined by trivial numerical tests beforehand and D_s is the total length of the damping zone in the direction of wave propagation. In this study, k_s and D_s are 15 and 3 m, respectively, by which the internal wave reflection can be absorbed.

The governing equations (2a)-(2b) and VOF equation (6) are solved using the finite volume method integrated in the OpenFOAM package. The velocity and pressure are decoupled by the Pressure Implicit with Splitting of Operators algorithm (PISO, Issa 1986). The Euler method is used to discretize the transient term. The convection term and diffusion term are discretized by the Gauss Limited Linear method and Gauss Linear Corrected method, respectively. For the details of the numerical implementations in OpenFOAM, see Jasak (1996) and Rusche (2003). The numerical computations always start from the still state, which means the static water pressure and zero velocity are specified as the initial conditions. The no-slip boundary condition is imposed at the solid wall, including the body surface and seabed surface. At the upper boundary of the numerical wave flume, a reference pressure $p = 0$ and the velocity condition for $\frac{\partial \mathbf{u}}{\partial \mathbf{n}}$ are implemented with $\mathbf{n}$ the outward normal unit vector. At the two ends of the spongy layer, zero velocities are applied considering that the waves are damped out there by the spongy layer. In the present numerical simulation, the time increment is automatically determined according to the Courant-Friedrichs-Lewy (CFL) condition,

$$\Delta t \leq C_r \times \min\{\sqrt{S_e}/|u_e|\}, \tag{10}$$

where S_e and $|u_e|$ are the area and absolute velocity in a computational cell, respectively. The numerical tests in this work confirmed that the use of $C_r = 0.20$ can produce stable and accurate results.

The classical linear potential flow model is also adopted in this study for the purpose of comparison. The boundary integral equation based on the Rankine source is developed for the problem, which has been described in the previous work in Jiang et al. (2019b). The higher-order boundary element method (HOBEM) with quadratic isoparametric elements (Teng and Eatock Taylor, 1995) is employed to discrete the boundary integral equation, of which the well-known formulation is omitted here.

3. Numerical Validations

As shown in Fig. 2, the two-dimensional fluid resonance in a moonpool formed by two identical rectangular hulls is considered in this work. The hulls with identical breadth $B = 0.360$ m and draft $D = 0.180$ m are located in the centre of the wave flume with the water depth $h = 1.03$ m. The moonpool between the hulls has the breadth $B_{mp} = 0.180$ m, where extremely large amplitude fluid resonances can be observed as the frequency of the hull motion is close to the natural frequency of the fluid bulk. In numerical simulations, a Cartesian coordinate system oxy is defined with the origin on the centre of the undisturbed free surface in the moonpool. The wave flume of 20 m in length and 1.5 m in height is adopted, where two spongy layers of 3.0 m long are situated on both ends of the wave flume for absorbing reflection waves. Four wave gauges are equipped to record the wave evolutions, where two of these, $G1_L$ and $G1_R$, are situated in the moonpool with the coordinates $x = \pm 0.08$ m and the other two wave gauges, $G2_L$ and $G2_R$, are placed at $x = \pm 1.150$ m, respectively. In this work, the averaged free surface amplitudes between the wave gauges $G1_L$ and $G1_R$ and wave gauges $G2_L$ and $G2_R$ are denoted as $G1$ and $G2$, respectively. The synchronous displacement of the twin hulls follows the heave and roll motions, respectively,

$$\xi_h(t) = A_b \sin(\omega t) \tag{11a}$$

$$\xi_r(t) = \alpha_b \sin(\omega t) \tag{11b}$$

where A_b and α_b are the heave and roll motion amplitudes, respectively; ω is the dimensional excitation frequency and the corresponding dimensionless excitation frequency is defined as $\Omega = \omega^2 B_{mp}/g$. The centre of rotation is fixed on the centre of the undisturbed free surface in the moonpool for roll motion excitations.

Numerical convergent tests are carried out by four different mesh schemes. To save computational costs, non-uniform meshes are adopted to discretise the computational domain. Roughly speaking, the square fine meshes with high resolution are utilized around the hulls to accurately capture the extreme wave resonance, especially in the vicinity of the moonpool. The coarse rectangular meshes with a large aspect ratio up to 1/20 (height/length) are adopted in both the left and right relaxation zones. The square fine meshes with intermediate resolution are equipped in the other parts of the computational domain. Details of different

Accepted to Phys. Fluids 10.1063/5.0180850

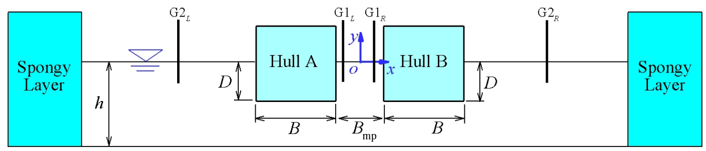

Figure 2: Sketch of the definition of the numerical wave flume.

meshes are tabulated in Tab. 1. Typical mesh partitions around the twin hulls are depicted in Fig. 3, which is Mesh 1 in Tab. 1.

Table 1: Detailed information of four different mesh schemes for the mesh convergence study.

Parameters	Physical meaning	Mesh 1	Mesh 2	Mesh 3	Mesh 4
N_x	No. of meshes along moonpool breadth B_{mp}	20	30	40	60
N_y	No. of meshes along box draft D	20	30	40	60
δy_{min}	Minimal mesh height on free surface (mm)	6.00	4.00	3.00	2.00
	Total number of cells in computational domain	8188	18300	32672	72800
	Total number of points in computational domain	16968	37490	66534	147378

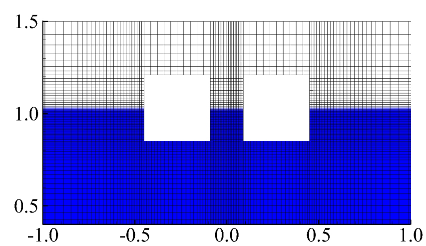

Figure 3: Typical computational meshes in the vicinity of the twin hulls .

Fig. 4 shows the free surface amplitudes at the wave gauge $G1$ in the moonpool by various mesh schemes, where the heave motion with $A_b = 0.050$, 0.0091 m and $\Omega = 0.50$, and the roll motion with $\alpha_b = 0.05$, 0.100 rad and $\Omega = 3.00$ are considered, respectively. Numerical simulations show that the convergent results can be produced by Mesh 3 because very little difference between the results of Mesh 3 and Mesh 4 can be observed. Therefore, Mesh 3 is adopted as the baseline for the following numerical simulations in this study.

The present numerical wave flume is validated against the experimental data in Faltinsen et al. (2007) for the twin hulls undergoing heave motion excitations. In their experiment, the moonpool tests were performed

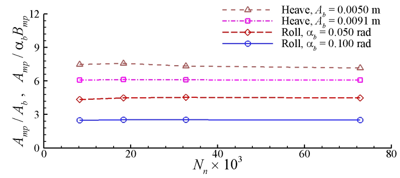

Figure 4: Free surface amplitudes in the moonpool at various heave and roll motions for the mesh convergent test.

in the narrow-wave flume of the Norwegian University of Science and Technology. The flume is 13.5 m long, 0.6 m wide and 1.03 m deep. The vertical regular oscillating motion of twin boxes was achieved by the use of a servo motor connected to a ball screw and rail system. As shown in Fig. 5, the comparison of wave responses in the moonpool at $G1$ and outside of the hulls at $G2$ under two heave amplitudes $A_b = 2.5$ mm and 5.0 mm is conducted, where the linear potential flow solutions are also included for comparison. Numerical results suggest that the resonant frequency in the moonpool can be predicted well by both the viscous fluid flow and potential flow models. The free surface amplitude A_{mp}/A_b in the moonpool predicted by the viscous fluid flow model is found to be in better agreement with the experimental data. However, the potential flow model significantly over-predicts the A_{mp}/A_b around the resonant frequency. It is known that the assumption of inviscid fluid and irrotational flow in the potential flow model is the major reason for the discrepancy. As for the predictions of radiation waves at $G2$, denoted by A_r/A_b, both the numerical results and the experimental data show that the largest radiation wave appears around the resonant frequency of the fluid oscillation in the moonpool. The maximal wave amplitude at $G2$ predicted by the potential flow model is slightly larger than those by the experimental test and viscous fluid flow model. The results of phase shifts to the excitations in Fig. 5 also show the superior agreement between the viscous fluid flow simulation and the laboratory measurement. In the potential flow results, little discrepancy with the experimental results can be observed at $G1$, while it over-predicts the phase shift at the gauge $G2$ (note that θ_r in the potential flow model is allowed to be larger than 2π in a small range to avoid a sudden jump in the phase shift).

4. Nonlinear behaviour of fluid resonance induced by fixed-amplitude roll motions

The validation study in the previous section shows that the present viscous fluid flow model is able to reproduce well the scenario of fluid resonance in the moonpool, which is adopted to investigate the free surface motion induced by two rectangular hulls undergoing roll motion excitations. Three sets of roll motion amplitudes, $\alpha_b = 0.025$, 0.050, 0.100 rad, are considered. Based on the linear potential flow analysis, the roll-motion induced sloshing-mode resonant frequency is $\Omega_n = 3.14$. In viscous fluid flow simulations, the dimensionless roll motion frequencies Ω range from 2.0 to 4.0, where the sloshing-mode resonance in the moonpool can be aroused. Finally, all the wave amplitudes presented in this section are evaluated *in the*

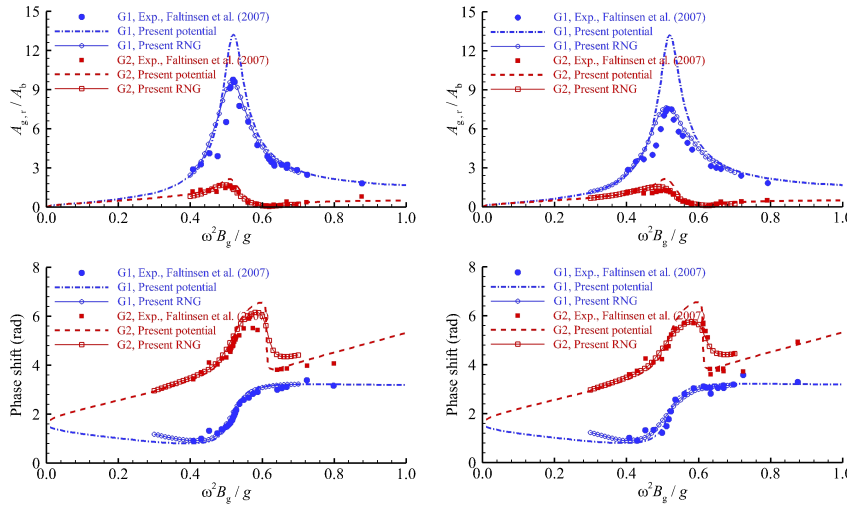

(a) $A_b = 2.5$ mm (b) $A_b = 5.0$ mm

Figure 5: Comparisons of wave amplitudes and phase shifts at G1 and G2 against the heave frequency for twin hulls at two different excitation amplitudes.

space-fixed coordinate system.

Fig. 6 shows the variation of wave amplitude at the wave gauge $G1$ with the roll motion frequency by the present viscous fluid flow model and the linear potential flow model. Numerical results obtained by the two different models show remarkably different behaviour in the figure. In the linear potential flow results, the significant increase of wave amplitude in the moonpool can be observed at the corresponding sloshing-mode resonant frequency which is $\Omega_n = 3.14$ in these figures. When the roll motion frequency becomes smaller or larger than the resonant frequency, i.e., $\Omega < \Omega_n$ or $\Omega > \Omega_n$, the continuously increased or decreased free surface amplitudes in the moonpool can be observed. It is a typical response behaviour of the linear mass-spring system. However, in the results of the viscous fluid flow model, the free surface amplitude abruptly increases from a relatively quiet state at the jump frequency and then the amplitude decreases gradually with the increase of roll motion frequency. The jump frequency is also the corresponding frequency of the maximal free surface amplitude in the moonpool, which is also the sloshing-mode resonant frequency predicted by the viscous fluid flow model. Furthermore, the resonant frequency predicted by the viscous fluid flow model is smaller than that by the linear potential flow model. The above phenomena indicate that the free surface response in the moonpool exhibits a softening spring behaviour, implying that the nonlinearity plays an important role in the sloshing-mode resonance under roll motion excitations. This is a realistic physical phenomenon and can be simulated by the viscous fluid flow model, correctly.

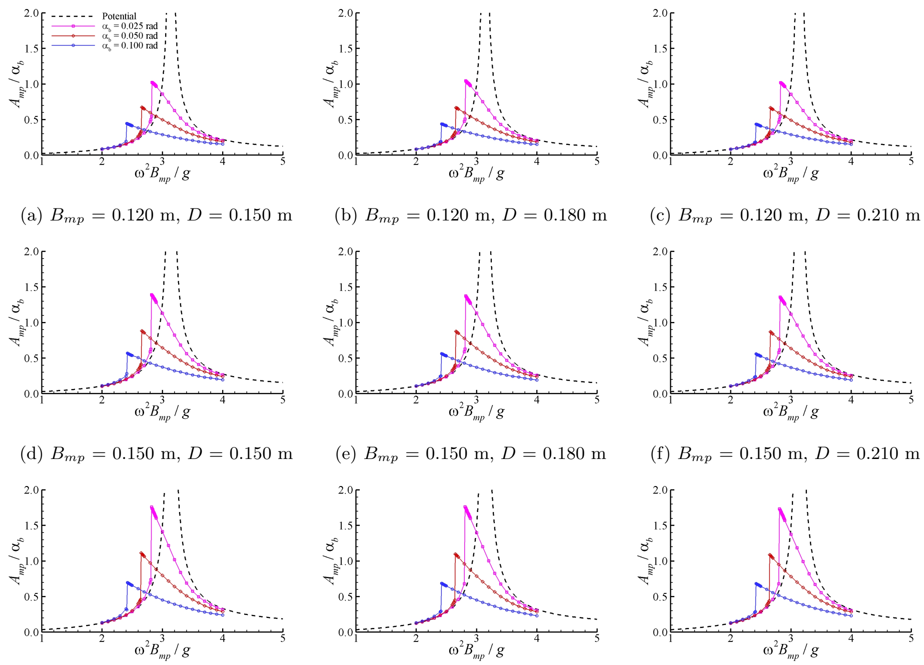

(a) $B_{mp} = 0.120$ m, $D = 0.150$ m (b) $B_{mp} = 0.120$ m, $D = 0.180$ m (c) $B_{mp} = 0.120$ m, $D = 0.210$ m

(d) $B_{mp} = 0.150$ m, $D = 0.150$ m (e) $B_{mp} = 0.150$ m, $D = 0.180$ m (f) $B_{mp} = 0.150$ m, $D = 0.210$ m

(g) $B_{mp} = 0.180$ m, $D = 0.150$ m (h) $B_{mp} = 0.180$ m, $D = 0.180$ m (i) $B_{mp} = 0.180$ m, $D = 0.210$ m

Figure 6: Free surface amplitudes at $G1_L$ under fixed-amplitude roll motion excitations with different dimensionless excitation frequencies Ω.

Accepted to Phys. Fluids 10.1063/5.0180850

Furthermore, with the increase of roll motion amplitude, the variation tendency of the relative amplitude A_{mp}/α_b in the viscous fluid flow results deviate more from the potential flow solutions, including both the decreased relative resonant amplitude and the increased resonance shift. For the softening spring system in this case, the increased resonance shift is equivalent to the decreased dimensionless resonant frequency (or jump frequency). It implies the increased influence of nonlinearity on the roll-motion induced sloshing-mode resonance in the moonpool. This increased nonlinear effect with the roll motion amplitude can also be explained by the nonlinear vibration theory. For the softening spring system, the decreased jump frequency can be generated by Eq. (1) with the increased coefficient $|\varepsilon|$ (absolute value) in the cubic nonlinear term. The increased coefficient $|\varepsilon|$ causes the increased effect of the cubic nonlinear term εx^3, further demonstrating that the increased roll motion amplitude increases the nonlinear action in the mass-spring system.

Fig. 7 shows the phase shifts of the free surface in the moonpool at different roll motion frequencies and amplitudes. The phase shifts predicted by the linear potential flow model only have two values, that is, π and 2π, where the corresponding frequency of sudden change in the phase shift is the resonant frequency. In the results of the viscous fluid flow model, the decreased resonant frequency (jump frequency) can also be observed, which is in accordance with the results of the free surface amplitudes. Refer to the sketch in Fig. 1, the jump frequency is due to the unstable solutions of the Duffing equation. It has the essential difference with the saltation in the linear potential flow solutions. Finally, Tab. 2 illustrates the values of dimensionless jump frequencies for the free surface responses at different moonpool geometries. For a specific roll motion amplitude, the moonpool geometries, including the moonpool breadth and draft, have an insignificant effect on the dimensionless jump frequency Ω_n. Further comparison in Fig. 6 indicates that the moonpool draft has an insignificant effect on the resonant amplitude; while the increased moonpool breadth is able to generate the increased free surface amplitude at resonant frequencies.

Table 2: Dimensionless jump frequencies Ω_n of free surface responses in the moonpool under different fixed-amplitude roll motions. ($\alpha_b = 0.025$ rad / $\alpha_b = 0.050$ rad / $\alpha_b = 0.100$ rad)

	$B_{mp} = 0.120$ m	$B_{mp} = 0.150$ m	$B_{mp} = 0.180$ m
$D = 0.150$ m	2.83 / 2.66 / 2.41	2.82 / 2.66 / 2.42	2.82 / 2.65 / 2.42
$D = 0.180$ m	2.82 / 2.66 / 2.42	2.82 / 2.66 / 2.42	2.81 / 2.65 / 2.42
$D = 0.210$ m	2.83 / 2.66 / 2.42	2.82 / 2.66 / 2.42	2.81 / 2.65 / 2.42

5. Hysteresis of fluid response by varying-amplitude roll motions

Numerical simulations are carried out to further investigate the hydrodynamic behaviour under varying roll motion amplitudes. For the purpose of illustration, the geometry of $B_{mp} = 0.180$ m and $D = 0.180$ m is adopted. Note that the jump frequencies are $\Omega_n = 2.81$, 2.65 and 2.42 for $\alpha_b = 0.025$, 0.050 and 0.100 rad,

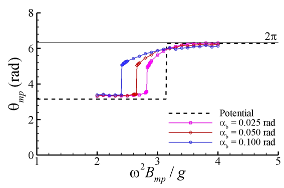

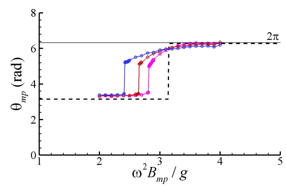

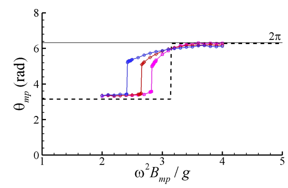

(a) $B_{mp} = 0.120$ m, $D = 0.150$ m (b) $B_{mp} = 0.120$ m, $D = 0.180$ m (c) $B_{mp} = 0.120$ m, $D = 0.210$ m

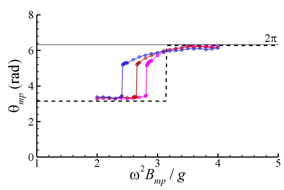

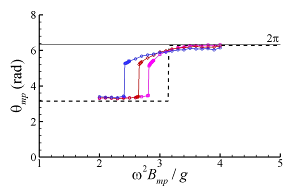

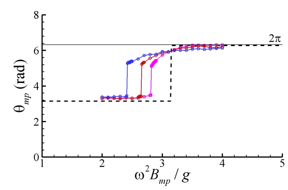

(d) $B_{mp} = 0.150$ m, $D = 0.150$ m (e) $B_{mp} = 0.150$ m, $D = 0.180$ m (f) $B_{mp} = 0.150$ m, $D = 0.210$ m

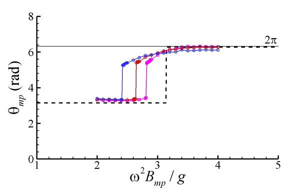

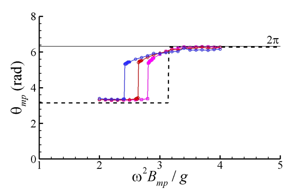

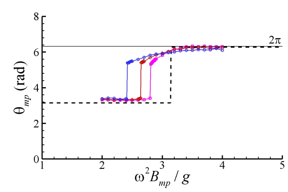

(g) $B_{mp} = 0.180$ m, $D = 0.150$ m (h) $B_{mp} = 0.180$ m, $D = 0.180$ m (i) $B_{mp} = 0.180$ m, $D = 0.210$ m

Figure 7: Phase shifts in $G1_L$ under fixed-amplitude roll motion excitations with different dimensionless frequency Ω.

respectively. In this study, the roll motion excitation with varying amplitudes is defined as follows,

$$\xi_r(t)=\begin{cases}\alpha_b^{(1)}\sin(\omega t), & t/T<n,\\ \gamma(\alpha_b^{(2)}-\alpha_b^{(1)})\sin(\omega t), & n<t/T<n+m,\\ \alpha_b^{(2)}\sin(\omega t), & t/T>n+m, \qquad n,m=1,2,3,\cdots.\end{cases} \tag{12}$$

where $T=2\pi/\omega$ is the period of roll motion excitation. $\alpha_b^{(1)}$ and $\alpha_b^{(2)}$ are defined as the amplitudes of the first and second stages in varying-amplitude roll motion excitations, respectively. γ is a linear ramp function to modulate the two stages of the varying-amplitude roll motion excitation. The values of n and m are used to control the duration of the first stage, transient and second stage. In this study, two types of varying-amplitude roll motion excitations, that is, accelerating excitation ($\alpha_b^{(1)}<\alpha_b^{(2)}$) and decelerating excitation ($\alpha_b^{(1)}>\alpha_b^{(2)}$), are considered. Fig. 8 illustrates a typical varying-amplitude roll motion signal of the accelerating and decelerating excitations. In the figure, the roll motion amplitudes of the first and second stages for the accelerating excitation are $\alpha_b^{(1)}=0.025$ rad and $\alpha_b^{(2)}=0.050$ rad, respectively; while they are $\alpha_b^{(1)}=0.100$ rad and $\alpha_b^{(2)}=0.050$ rad for the decelerating excitation. That is, the difference between the accelerating and decelerating excitations is only the first stage amplitude, while the roll motion amplitudes of the second stage are the same as each other. To avoid the transients between the two stages, the ramp function γ is applied for five wave periods (i.e. $m=5$). Numerical simulations have demonstrated that the ramp function has an insignificant effect on the results of free surface responses.

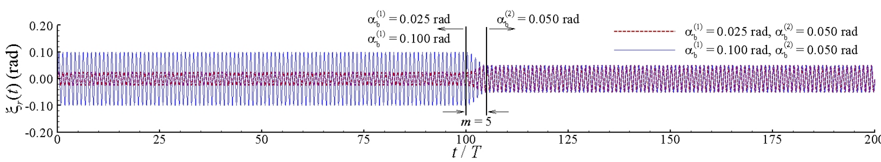

Figure 8: Typical roll motion signals of accelerating and decelerating excitations.

Fig. 9 shows the comparison of free surface evolutions in the moonpool at the wave gauge $G1_L$ between the accelerating and decelerating excitations at four sets of dimensionless frequencies, $\Omega=2.00$, 2.45, 2.60 and 3.00. It is observed that the amplitudes of free surface elevations increase gradually at the initial stage. After a short transient, the steady-state evolutions can be observed at the first stage. The amplitudes at the first stage between the accelerating and decelerating excitations are different, because different roll motion amplitudes, i.e., $\alpha_b^{(1)}=0.025$ and 0.100 rad, can generate different free surface responses in the moonpool. At the second stage, the relationship of free surface responses between the accelerating and decelerating excitations shows different characteristics at different excitation frequencies, even the accelerating and decelerating excitations have the same amplitude at this stage. In Figs. 9a and 9d at $\Omega=2.00$ and 3.00, the increased and decreased free surface amplitudes in the moonpool can be observed during the transient period in the accelerating and decelerating results. With the elapse of time, the free surface evolutions by the accelerating and decelerating excitations almost coincide completely with each other. The same roll motion amplitudes, i.e., $\alpha_b^{(2)} = 0.050$ rad, at the second stage are able to generate the same free surface responses in the moonpool, implying that there is no hysteresis phenomenon at these two frequencies.

Fig. 9c shows the free surface evolution in the moonpool at the dimensionless roll motion frequency $\Omega = 2.60$. The averaged amplitudes at the first stage between the dimensionless duration of t/T = 25 - 75 are $A_{mp}^{(1)} = 8.549$ mm and 60.014 mm for the accelerating and decelerating excitations, respectively. At the second stage, the steady-state averaged amplitude in the moonpool by the accelerating excitation between the dimensionless duration of t/T = 130 - 180 is $A_{mp}^{(2)} = 18.990$ mm. It is very close to the results of the fixed rolling amplitude $\alpha_b = 0.050$ rad, where the corresponding averaged free surface amplitude in the moonpool is $A_{mp} = 19.191$ mm. However, in the decelerating results, the steady-state averaged amplitude at the second stage is $A_{mp}^{(2)} = 56.597$ mm, which only has a little decrease compared to the amplitude of $A_{mp}^{(1)} = 60.014$ mm at the first stage. Moreover, the above results indicate that the same roll motion amplitude at the second stage, i.e., $\alpha_b^{(2)} = 0.050$ rad, generates different free surface responses ($A_{mp}^{(2)} = 18.990$ and 56.597 mm) in the moonpool under the decelerating and accelerating excitations. That is, the free surface response at the second stage is dependent on the roll motion excitation at the first stage, which is a typical 'Hysteresis' phenomenon.

Phase shifts at the first and second stages are also considered in Fig. 9c. In the accelerating results, the phase shifts at the wave gauge $G1_L$ are $\theta_{mp}^{(1)} = 3.386$ rad and $\theta_{mp}^{(2)} = 3.392$ rad between the dimensionless durations of t/T = 25 - 75 and 130 - 180 at the first and second stages, respectively. Again, it is very close to the results of the fixed rolling amplitude $\alpha_b = 0.050$ rad, where the corresponding phase shift is $\theta_{mp} = 3.393$ rad. The above results indicate the phase shifts for $\alpha_b = 0.025$ rad and 0.050 rad are nearly the same as each other. Therefore, the increase of roll motion amplitude is able to generate the increased free surface amplitude in the moonpool when the excitation is from $\alpha_b^{(1)} = 0.025$ at the first stage to $\alpha_b^{(2)} = 0.050$ at the second stage. However, the phase shift between the dimensionless duration of t/T = 25 - 75 in the decelerating results is $\theta_{mp}^{(1)} = 5.579$ rad for $\alpha_b^{(1)} = 0.100$ rad at the first stage, which is very different to $\theta_{mp} = 3.393$ for the fixed roll motion amplitude $\alpha_b = 0.050$ rad. At the second stage with $\alpha_b^{(2)} = 0.050$ rad, the corresponding phase shift of the free surface response between the dimensionless duration of t/T = 130 - 180 is $\theta_{mp}^{(2)} = 5.113$ rad. It is much closer to $\theta_{mp}^{(1)} = 5.579$ rad at the first stage for the roll motion amplitude $\alpha_b^{(1)} = 0.100$ rad, but quite different to $\theta_{mp} = 3.393$ for the fixed roll motion amplitude $\alpha_b = 0.050$ rad. This implies the phase shift at the second stage is locked by that at the first stage, leading to the corresponding free surface amplitude at the second stage being nearly the same as that at the first stage. This is the essential reason for the above 'Hysteresis' phenomenon of free surface amplitudes in the moonpool under decelerating excitations.

Fig. 9b shows the comparison of free surface evolutions in the moonpool between the accelerating and decelerating excitations at the dimensionless roll motion frequency $\Omega = 2.45$. The free surface amplitudes are $A_{mp}^{(1)} = 6.434$ and $A_{mp}^{(2)} = 13.046$ mm in the accelerating results at the first and second stages, respectively;

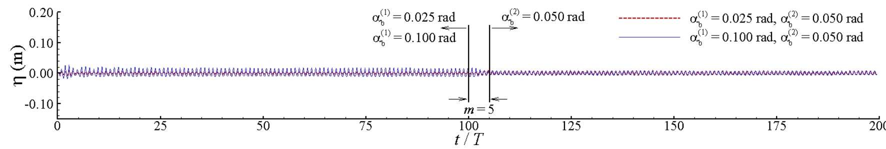

(a) $\Omega = 2.00$

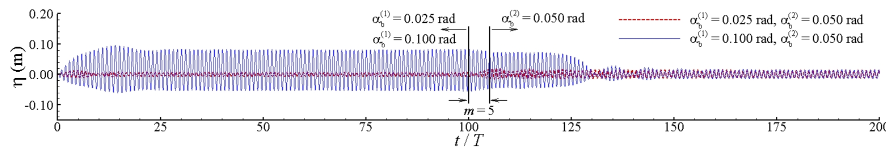

(b) $\Omega = 2.45$

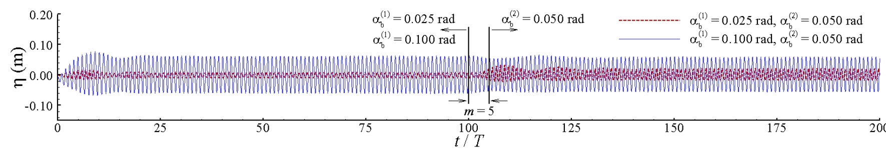

(c) $\Omega = 2.60$

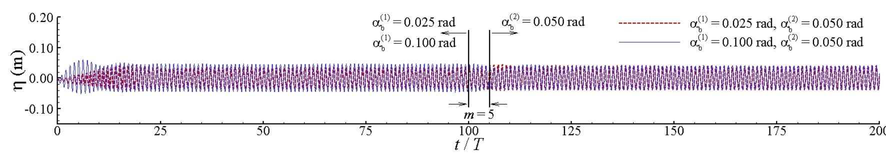

(d) $\Omega = 3.00$

Figure 9: Time histories of free surface evolutions in moonpool for $B_{mp} = 0.180$ m and $D = 0.180$ m under accelerating and decelerating excitations.

while the corresponding phases shifts are $\theta_{mp}^{(1)} = 3.325$ and $\theta_{mp}^{(2)} = 3.371$ rad, respectively. In the decelerating results, the free surface amplitude and phase shift at the first stage are $A_{mp}^{(1)} = 67.203$ mm and $\theta_{mp}^{(1)} = 5.408$ rad, respectively. At the second stage, the free surface amplitude and phase shift between the dimensionless duration of t/T = 105 - 120 are $A_{mp}^{(2)} = 58.621$ mm and $\theta_{mp}^{(2)} = 4.342$ rad, respectively, which are different to the results of $A_{mp}^{(2)} = 13.046$ mm and $\theta_{mp}^{(2)} = 3.371$ rad at the second stage by the accelerating excitation. This indicates the free surface response in the moonpool is dependent on the roll motion excitation at the first stage, implying the hysteresis phenomenon happens. However, the phase shift $\theta_{mp}^{(2)} = 4.342$ rad between t/T = 105 - 120 is not very close to $\theta_{mp}^{(1)} = 5.408$ rad at the first stage, which is not the locked-in phenomenon, strictly. Moreover, the above hysteresis phenomenon only lasts about 15 waves, that is, between the dimensionless durations of t/T = 105 - 120 in Fig. 9b. Then, the free surface amplitude decreases rapidly and the steady-state value is $A_{mp}^{(2)} = 13.485$ mm after a short transient. Correspondingly, the phase shift of the steady-state free surface response becomes $\theta_{mp}^{(2)} = 3.346$ rad. This indicates that the free surface response at the second stage under the decelerating excitation is the same as that under the accelerating excitation, which is confirmed by the coinciding time signals of the free surface response between the accelerating and decelerating results during t/T = 160 - 200 in Fig. 9b. The above phenomenon reveals the 'Hysteresis' cannot generate a stable effect on wave response in the moonpool at $\Omega = 2.45$. In addition, it also indicates that sufficient simulation time is important in this study.

Figs. 10 and 11 show the variation of free surface amplitudes and phase shifts at the second stage in the moonpool with varying-amplitude roll motion frequencies. In the simulations, the roll motion amplitude at the second stage is kept at $\alpha_b^{(2)} = 0.050$ rad. At the first stage, four sets of roll motion amplitudes, $\alpha_b^{(1)}$ = 0.005, 0.025, 0.100, and 0.150 rad, are adopted. The former two rolling excitations are the accelerating excitations; while the latter two rolling excitations are the decelerating excitations. For the purpose of comparison, numerical results for the fixed roll motion amplitude $\alpha_b = 0.050$ rad are also included, which is indicated as $\alpha_b^{(1)} = 0.050$ rad in these figures. Typical hysteresis loop can be observed in the figure, that is, free surface amplitudes $A_{mp}^{(2)}/\alpha_b^{(2)}$ and phase shifts $\theta_{mp}^{(2)}/\alpha_b^{(2)}$ in the moonpool have different values at some frequencies under accelerating and decelerating excitations, respectively. Further comparisons indicate that the results between $\alpha_b^{(1)} = 0.005$ and 0.025 rad in the accelerating excitations and the results between $\alpha_b^{(1)}$ = 0.100 and 0.150 rad in the decelerating excitations are the same as each other, respectively. That is, the accelerating and decelerating processes are able to generate the hysteresis phenomena; while the values of roll motion amplitudes at the first stage $\alpha_b^{(1)}$ in the accelerating or decelerating excitations cannot affect the final wave response in the moonpool. The results for $\alpha_b^{(1)} = 0.005$ and 0.025 rad are the same as the results for the fixed roll motion amplitude $\alpha_b = 0.050$ rad. It can be understood that the fixed roll motion amplitude α_b = 0.050 rad can also be considered as the accelerating excitation with $\alpha_b^{(1)} = 0$ and $\alpha_b^{(2)} = 0.050$ rad. Generally, experiments or simulations always begin from the static state in practical engineering, implying that the rolling response of the hull is always a zero-angle state. The obtained experimental or numerical results may underestimate the free surface amplitudes in the moonpool, leading to a possibly dangerous design at the

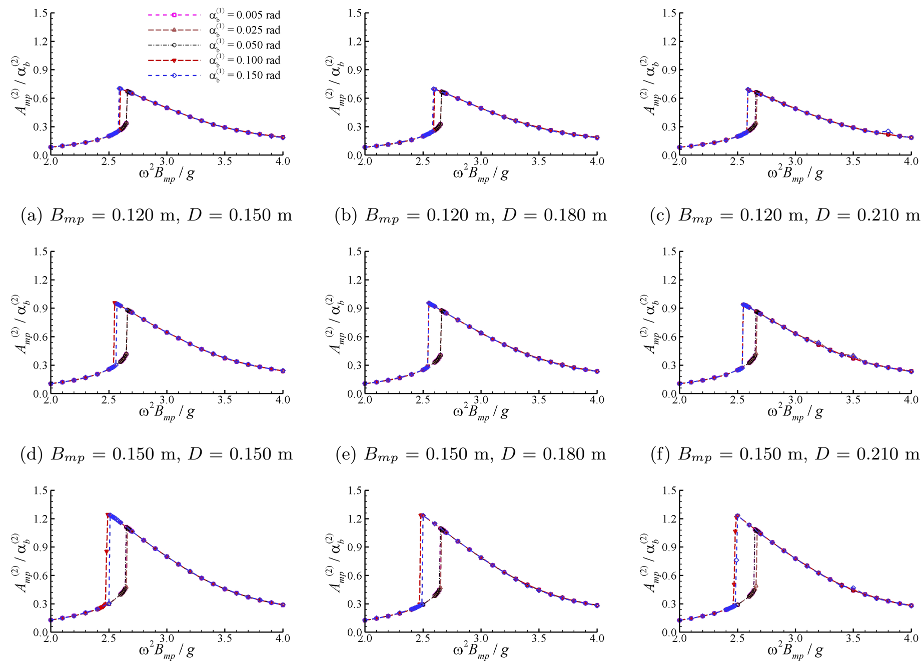

(a) $B_{mp} = 0.120$ m, $D = 0.150$ m (b) $B_{mp} = 0.120$ m, $D = 0.180$ m (c) $B_{mp} = 0.120$ m, $D = 0.210$ m

(d) $B_{mp} = 0.150$ m, $D = 0.150$ m (e) $B_{mp} = 0.150$ m, $D = 0.180$ m (f) $B_{mp} = 0.150$ m, $D = 0.210$ m

(g) $B_{mp} = 0.180$ m, $D = 0.150$ m (h) $B_{mp} = 0.180$ m, $D = 0.180$ m (i) $B_{mp} = 0.180$ m, $D = 0.210$ m

Figure 10: Free surface amplitudes in $G1_L$ under varying-amplitude roll motion excitations at different dimensionless frequencies Ω.

frequency range of the hysteresis loop.

The frequency range of the hysteresis loop, which can be identified between two jump frequencies in Figs. 10 and 11, is considered. It can be observed that the jump frequency induced by the accelerating excitations is larger than that by the decelerating excitations. Correspondingly, the free surface amplitude by the accelerating excitations follows the lower branch and the free surface amplitude by the decelerating excitations follows the upper branch. The free surface amplitudes and phase shifts by the accelerating excitations are smaller than those by the decelerating excitations in the region of the hysteresis loop. Furthermore, Tab. 3 tabulates dimensionless jump frequencies of the upper and lower branch in the hysteresis loop, where the accelerating excitation with $\alpha_b^{(1)} = 0.025$ rad and $\alpha_b^{(2)} = 0.050$ rad and the decelerating excitation with $\alpha_b^{(1)} = 0.100$ rad and $\alpha_b^{(2)} = 0.050$ rad are illustrated. According to the comparison with the results in Tab. 2 by the fixed-amplitude excitations, the jump frequencies of the lower branch under the accelerating excitation with $\alpha_b^{(1)} = 0.025$ rad and $\alpha_b^{(2)} = 0.050$ rad is nearly the same as that for the fixed roll motion amplitude $\alpha_b = 0.050$ rad. However, the jump frequencies of the upper branch under the decelerating excitations with

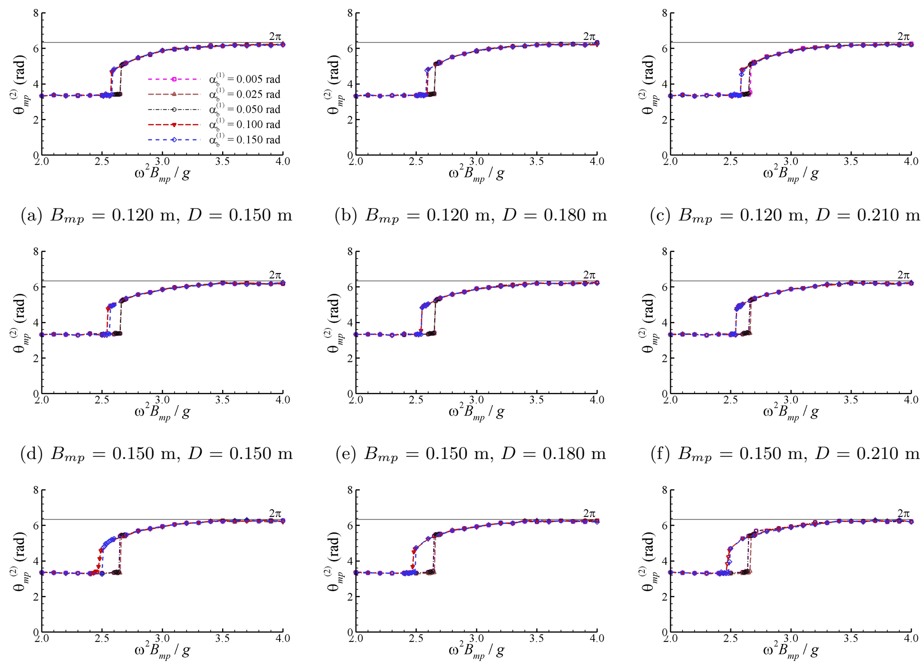

(a) B_{mp} = 0.120 m, D = 0.150 m (b) B_{mp} = 0.120 m, D = 0.180 m (c) B_{mp} = 0.120 m, D = 0.210 m

(d) B_{mp} = 0.150 m, D = 0.150 m (e) B_{mp} = 0.150 m, D = 0.180 m (f) B_{mp} = 0.150 m, D = 0.210 m

(g) B_{mp} = 0.180 m, D = 0.150 m (h) B_{mp} = 0.180 m, D = 0.180 m (i) B_{mp} = 0.180 m, D = 0.210 m

Figure 11: Phase shifts in $G1_L$ under varying-amplitude roll motion excitations at different dimensionless frequencies Ω.

$\alpha_b^{(1)} = 0.100$ rad and $\alpha_b^{(2)} = 0.050$ rad are always lower than that for the fixed roll motion amplitude $\alpha_b =$ 0.100 rad. This is mainly due to that the Hysteresis cannot generate a stable effect on the wave response at the corresponding frequencies, which has been explained in Fig. 9b. Finally, Tab. 3 also illustrates that the jump frequency of the upper branch decreases with the increase of the moonpool breadth, leading to a wider frequency range of the hysteresis loop for a larger moonpool breadth. However, it is nearly independent of the moonpool draft in these figures. This implies the influence of the hysteresis would have a wider frequency range with the increase of the moonpool breadth in practical engineering.

Table 3: Dimensionless jump frequencies Ω_n of upper and lower branches in the hysteresis loop by the accelerating excitation with $\alpha_b^{(1)} = 0.025$ rad and $\alpha_b^{(2)} = 0.050$ rad and the decelerating excitation with $\alpha_b^{(1)}$ = 0.100 rad and $\alpha_b^{(2)} = 0.050$ rad. (upper branch / lower branch)

	$B_{mp} = 0.120$ m	$B_{mp} = 0.150$ m	$B_{mp} = 0.180$ m
$D = 0.150$ m	2.60 / 2.66	2.55 / 2.66	2.49 / 2.65
$D = 0.180$ m	2.60 / 2.66	2.55 / 2.66	2.48 / 2.65
$D = 0.210$ m	2.59 / 2.66	2.55 / 2.66	2.48 / 2.65

6. Conclusion

Fluid resonance in the moonpool formed by twin hulls is investigated by using a viscous fluid flow with the RNG turbulent model based on the OpenFOAM® package. Numerical validations are carried out by comparison with the experimental and numerical results in the literature, confirming that the present model can work well in simulating the moonpool resonant behaviour. Nonlinearity plays an important role in the sloshing-mode resonance in the moonpool induced by the roll motion excitation, where a softening spring behaviour is reported. With the increase of roll motion amplitude, the increased effect of the nonlinearity can be observed. All of these phenomena can be explained by the Duffing equation. Hysteresis phenomena are reported in the free surface responses in the moonpool under the excitations with varying roll motion amplitudes. The phase locked-in is the essential reason for the results. The accelerating excitation is able to generate the lower branch of the hysteresis loop, where the jump frequency is independent of the geometries of the moonpool. The decelerating excitation can generate the upper branch frequency of the hysteresis loop, where the jump frequency decreases with the increase of moonpool breadth. It leads to the wider region of the hysteresis loop for larger moonpool breadths.

Acknowledgments

This work is supported by the National Natural Science Foundation of China with Grant Nos. 52171250 and 51909027. The first author gratefully acknowledges the Supercomputer Center of Dalian University of Technology for providing computing resources.

Data Availability

All data generated or analyzed during this study are included in this article.

References

Bäuerlein, B. and Avila, K. (2021). Phase lag predicts nonlinear response maxima in liquid-sloshing experiments, *Journal of Fluid Mechanics* **925**: A22.

Chu, B. and Zhang, X. (2021). On the natural frequencies and modal shapes in two-dimensional moonpools with recesses in finite water depth, *Applied Ocean Research* **115**: 102787.

Duffing, G. (1918). *Erzwungene Schwingungen bei veränderlicher Eigenfrequenz und ihre technische Bedeutung*, F. Vieweg & Sohn.

Faltinsen, O. M., Rognebakke, O. F., Lukovsky, I. A. and Timokha, A. N. (2000). Multidimensional modal analysis of nonlinear sloshing in a rectangular tank with finite water depth, *Journal of fluid mechanics* **407**: 201–234.

Faltinsen, O., Rognebakke, O. and Timokha, A. (2007). Two-dimensional resonant piston-like sloshing in a moonpool, *Journal of Fluid Mechanics* **575**: 359–397.

Faltinsen, O. and Timokha, A. (2015). On damping of two-dimensional piston-mode sloshing in a rectangular moonpool under forced heave motions, *Journal of Fluid Mechanics* **772**: R1.

Feng, X., Bai, W., Chen, X., Qian, L. and Ma, Z. (2017). Numerical investigation of viscous effects on the gap resonance between side-by-side barges, *Ocean Engineering* **145**: 44–58.

Fredriksen, A., Kristiansen, T. and Faltinsen, O. (2014). Experimental and numerical investigation of wave resonance in moonpools at low forward speed, *Applied Ocean Research* **47**: 28–46.

Fredriksen, A., Kristiansen, T. and Faltinsen, O. (2015). Wave-induced response of a floating two-dimensional body with a moonpool, *Philosophical Transactions of the Royal Society A: Mathematical, Physical and Engineering Sciences* **373**: 20140109.

Gao, J., Zang, J., Chen, L., Ding, H. and Liu, Y. (2019). On hydrodynamic characteristics of gap resonance between two fixed bodies in close proximity, *Ocean Engineering* **173**: 28–44.

Gardarsson, S. and Yeh, H. (2007). Hysteresis in shallow water sloshing, *Journal of engineering mechanics* **133**(10): 1093–1100.

Gurusamy, S. and Kumar, D. (2020). Experimental study on nonlinear sloshing frequency in shallow water tanks under the effects of excitation amplitude and dispersion parameter, *Ocean Engineering* **213**: 107761.

Gurusamy, S., Sanapala, V., Kumar, D. and Patnaik, B. (2021). Sloshing dynamics of shallow water tanks: Modal characteristics of hydraulic jumps, *Journal of Fluids and Structures* **104**: 103322.

Hill, D. F. (2003). Transient and steady-state amplitudes of forced waves in rectangular basins, *Physics of Fluids* **15**(6): 1576–1587.

Hirt, C. W. and Nichols, B. D. (1981). Volume of fluid (VOF) method for the dynamics of free boundaries, *Journal of Computational Physics* **39**(1): 201–225.

Issa, R. (1986). Solution of the implicitly discretised fluid flow equations by operator-splitting, *Journal of Computational Physics* **62**(1): 40–65.

Jasak, H. (1996). *Error analysis and estimation for the finite volume method with applications to fluid flows*, PhD thesis, Imperial College London.

Jiang, S., Bai, W. and Tang, G. (2018). Numerical simulation of wave resonance in the narrow gap between two non-identical boxes, *Ocean Engineering* **156**: 38–60.

Jiang, S., Bai, W. and Tang, G. (2019a). Numerical investigation of piston-modal wave resonance in the narrow gap formed by a box in front of a wall, *Physics of Fluids* **31**: 052105.

Jiang, S., Bai, W. and Yan, B. (2021). Higher-order harmonic induced wave resonance for two side-by-side boxes in close proximity, *Physics of Fluids* **33**: 102113.

Jiang, S. C., Ran, Y. Q. and Feng, A. (2023). On the hydrodynamic behaviour of second-order harmonic induced sloshing-mode resonance in moonpool, *Marine Structures* **92**: 103503.

Jiang, S., Cong, P., Sun, L. and Liu, C. (2019b). Numerical investigation of edge configurations on piston-modal resonance in a moonpool induced by heaving excitations, *Journal of Hydrodynamics* **31**(4): 682–699.

Jing, P. L., He, G. H., Luan, Z. X., Liu, C. G. and Yang, H. (2022). Numerical study of fluid resonance of a two-dimensional heaving-free moonpool in a wide range of incident waves, *Journal of Hydrodynamics* **34**(4): 647–664.

Kovacic, I. and Brennan, M. J. (2011). *The Duffing equation: nonlinear oscillators and their behaviour*, John Wiley & Sons, Ltd.

Liu, D., Wu, Y. and Lin, P. (2022). An experimental study of two-layer liquid sloshing under pitch excitations, *Physics of Fluids* **34**: 052112.

Lu, L., Cheng, L., Teng, B. and Zhao, M. (2010). Numerical investigation of fluid resonance in two narrow gaps of three identical rectangular structures, *Applied Ocean Research* **32**: 177–190.

Lu, L., Tan, L., Zhou, Z., Zhao, M. and Ikoma, T. (2020). Two-dimensional numerical study of gap resonance coupling with motions of floating body moored close to a bottom-mounted wall, *Physics of Fluids* **32**: 092101.

Miliaiev, A. and Timokha, A. (2023). Viscous damping of steady-state resonant sloshing in a clean rectangular tank, *Journal of Fluid Mechanics* **965**: R1.

Milne, I., Kimmoun, O., Graham, J. and Molin, B. (2022). An experimental and numerical study of the resonant flow between a hull and a wall, *Journal of Fluid Mechanics* **930**: A25.

Molin, B. (2001). On the piston and sloshing modes in moonpools, *Journal of Fluid Mechanics* **430**: 27–50.

Molin, B., Zhang, X., Huang, H. and Remy, F. (2018). On natural modes in moonpools and gaps in finite depth, *Journal of Fluid Mechanics* **840**: 530–554.

Ockendon, H. and Ockendon, J. (2001). Nonlinearity in fluid resonances, *Meccanica* **36**: 297–321.

Rusche, H. (2003). *Computational fluid dynamics of dispersed two-phase flows at high phase fractions*, PhD thesis, Imperial College London.

Tan, L., Lu, L., Tang, G., Cheng, L. and Chen, X. (2019). A viscous damping model for piston mode resonance, *Journal of Fluid Mechanics* **871**: 510–533.

Teng, B. and Eatock Taylor, R. (1995). New higher-order boundary element methods for wave diffraction/radiation, *Applied Ocean Research* **17**(2): 71–77.

Yakhot, V. and Orszag, S. (1986). Renormalization group analysis of turbulence. I. Basic theory, *Journal of Scientific Computing* **1**(1): 3–51.

Yakhot, V. and Smith, L. M. (1992). The renormalization group, the ε-expansion and derivation of turbulence models, *Journal of Scientific Computing* **7**(1): 35–61.

Zhang, X., Huang, H. and Song, X. (2019). On natural frequencies and modal shapes in two-dimensional asymmetric and symmetric moonpools in finite water depth, *Applied Ocean Research* **82**: 117–129.

Zhang, X. and Li, Z. (2022). Natural frequencies and modal shapes of three-dimensional moonpool with recess in infinite-depth and finite-depth waters, *Applied Ocean Research* **118**: 102921.